Supporting Information

Oxygen-bridged electronic coupling of Ir single-atom sites for durable acidic oxygen evolution reaction

Yijun Xiang,[a] Hui Wang,[b] Shaoxiong Li,[a] Linlin Li,[a] Jianwei Ren,[c] Gengyu Xing,*[a] Liming Deng,*[a] and Shengjie Peng*[d]

[a] College of Materials Science and Technology, Nanjing University of Aeronautics and Astronautics, Nanjing 210016, China

[b] Xi'an Aerospace Propulsion Institute, Xi'an 710100, China.

[c] Department of Chemical Engineering, University of Pretoria, Pretoria 0028, South Africa

[d] School of Energy and Environment & Z Energy Storage Center, Southeast University, Nanjing 211189, China

Electrochemical measurements

The catalyst loading on the carbon paper was controlled at approximately 0.5 mg cm^{-2}. The measured potentials versus Ag/AgCl were converted to the reversible hydrogen electrode (RHE) according to the equation:

$$E_{RHE} = E_{Ag/AgCl} + 0.197V + 0.0591 \times pH \quad (1)$$

The linear sweep voltammetry (LSV) polarization curves were recorded at a scan rate of 5 mV s^{-1} with 100% iR compensation. The uncompensated resistance (R_n) used for iR correction was obtained from the high-frequency intercept of the Nyquist plots recorded by electrochemical impedance spectroscopy (EIS). To minimize interference from double-layer capacitance, all EIS measurements for iR compensation were performed at low current densities (< 0.1 mA cm^{-2}). Electrochemical impedance spectroscopy (EIS) was performed over 0.01−100 kHz with an AC amplitude of 5 mV. The double-layer capacitance (C_{dl}) was obtained by collecting CV curves with scan rates of 20 to 100 mV s^{-1}.

Calculation of the specific current density normalized to the electrochemically active surface area (ECSA). The electrochemical double-layer capacitance (C_{dl}) was obtained by evaluating the capacitive current arising from double-layer charging, as determined from cyclic voltammetry at varying scan rates. C_{dl} was further calculated by plotting $\Delta j = (j_a - j_c)$, where j_a and j_c denote the anodic and cathodic current densities, respectively, as a function of scan rate, with the slope corresponding to twice the C_{dl} value.

The turnover frequency (TOF) of the catalysts was calculated using the following equation:

$$TOF(s^{-1}) = \frac{\text{oxygen turnovers per } A_{geo}}{\text{active sites per } A_{geo}} \quad (2)$$

The oxygen turnover per geometric area was derived from the geometric current density for the LSV polarization curves according to the equation:

$$oxygen\ turnover\ per\ A_{geo} = j_{geo} \times \frac{1\ C\ s^{-1}}{1000\ mA} \times \frac{1\ mol}{96485.3\ C} \times \frac{1}{4} \times \frac{6.023 \times 10^{23}}{1 mol\ O_2} \quad (3)$$

Electrochemical impedance spectroscopy (EIS) was used to analyze electrode kinetics, double-layer capacitance, and diffusion processes. The impedance spectra were fitted with an equivalent circuit consisting of R_1, R_2, and C_1. Here, R_1 represents the electrolyte resistance, R_2 corresponds to the charge-transfer resistance, and C1 is modeled as a constant phase element (CPE). The CPE is described by two parameters, CPE-T (Q) and CPE-P (n), where Q is the pseudo-capacitance factor and n ($0 < n < 1$) reflects the deviation from ideal capacitive behavior. The effective capacitance (C_Φ) was calculated from the fitted CPE parameters

using the relation:

$$C_{\phi} = Q^{1/n} \quad (4)$$

which was then employed to evaluate the intermediate accumulation capability at different applied potentials.

Pulse voltammetry (PV) was performed while recording the current as a function of time (1,600 rpm RDE). The potential was first held at a low potential (E_l = 1.35 V vs. Ag/AgCl), then stepped to a higher potential (E_h) before returning to E_l. This cycle was repeated by increasing Eh from 1.38 V to 1.72 V in 20 mV increments, while E_l remained constant. The charge associated with each potential step was calculated by integrating the current pulse over time after subtracting the background current.

PEMWE measurements

The cell voltage, Ecell, consists of the reversible cell potential together with the major overpotentials:

$$E_{cell} = E_{rev}^{0} + \eta_{kin} + \eta_{\Omega} + \eta_{mt} \quad (5)$$

where η_{kin} is the kinetic overpotential, η_{Ω} is the ohmic overpotential, and η_{mt} is the mass-transport overpotential. As the HER is more favorable in terms of kinetics and mass transport under the present testing conditions compared to the OER, the overpotential analysis focused only on the OER side.

At 80 °C, the saturation vapor pressure of H_2O is 0.47 bar. For liquid water, activity a(H_2O) is defined as 1, whereas the activity of gaseous species is represented by the ratio of their partial pressure to the standard state of 1 bar. The temperature-dependent standard reversible potential for the overall water-splitting reaction can be expressed as:

$$E_{rev}^{0} = 1.2291 - 0.0008456 \times (T - 298.15) \quad (6)$$

where the voltages (the first two terms on the right-hand side of the equation) are in V, and the temperatures are given in K. Under the current electrolyzer operating conditions, the E_{rev}^{0} was estimated to be 1.168 V, with a thermoneutral potential of 1.42 V.

EIS measurements were used to determine the high-frequency resistance (HFR), representing the total cell resistance R_{tot}. The ohmic overpotential, η_{Ω}, was therefore calculated as:

$$\eta_{\Omega} = i \times HFR \quad (7)$$

The kinetic overpotential was obtained by fitting the iR-free PEMWE polarization curves to the Tafel model, in which the Tafel slope b and the exchange current density i_0 are the governing kinetic parameters. The Tafel slope b is given as 2.303 × RT/4F, where R is the universal gas constant, T is the temperature, and F is Faraday's constant. Assuming a non-polarizable HER, the overall kinetic loss of the cell was attributed to the OER, with η_{kin} expressed as:

$$\eta_{\text{kin}} = b\log\left(\frac{i}{i_0}\right) \quad (8)$$

Mass-transport overpotential was defined as the combined contribution of gas/liquid transfer in the PTL/CL and ionic transport within the CLs. In this study, it was calculated by subtracting the reversible potential, ohmic, and kinetic overpotentials from the measured cell voltage.

Theoretical calculation

All DFT calculations were performed using the Vienna Ab initio Simulation Package (VASP).[1] The projector augmented wave (PAW) pseudopotential, along with the Perdew-Burke-Ernzerh (PBE) generalized gradient approximation (GGA) exchange-correlation function, was utilized in the computations.[2-3] All energetics of metal oxides were calculated using the DFT with the Hubbard-U framework (DFT+U) to account for strongly localized d-electrons for Co. The Hubbard-U correction terms were at U_{eff}(Co) = 3.32 eV, as obtained via linear response theory. The cutoff energy of the plane wave basis set was 500 eV, and a Monkhorst-Pack mesh of 3×3×1 was used in K-sampling. All structures were spin polarized, and all atoms were fully relaxed with the energy convergence tolerance of 10^{-5} eV per atom, and the final force on each atom was < 0.05 eV $Å^{-1}$.

The adsorption energy of reaction intermediates, can be computed using the following Equation:

$$\Delta G_{ads} = E_{ads} - E_{*} + \Delta E_{ZPE} - T\Delta S \quad (9)$$

Where ads = (OH*, O* and OOH*), and ($E_{ads} - E_{*}$) is the binding energy, ΔE_{ZPE} is the zero-point energy change, ΔS is the entropy change. In this work, the values of ΔE_{ZPE} and ΔS were obtained by vibration frequency calculation.

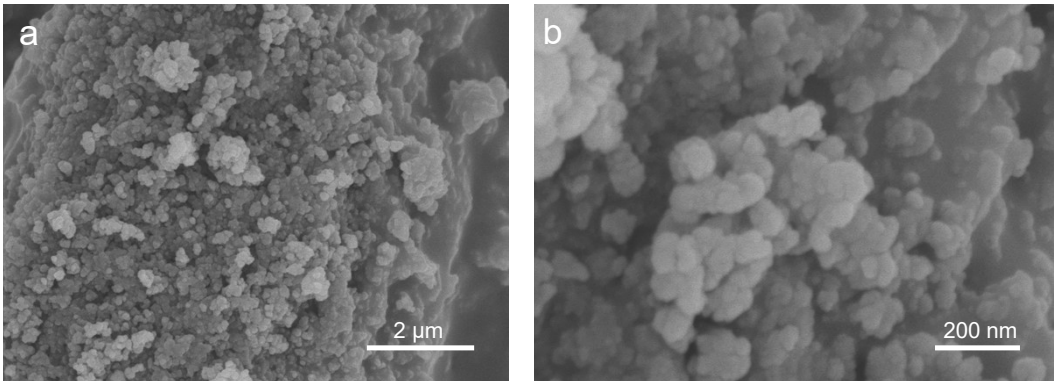

Fig. S1. (a) Low-magnified and (b) high-magnified SEM images of glycerolatocobalt (Co-gly), respectively.

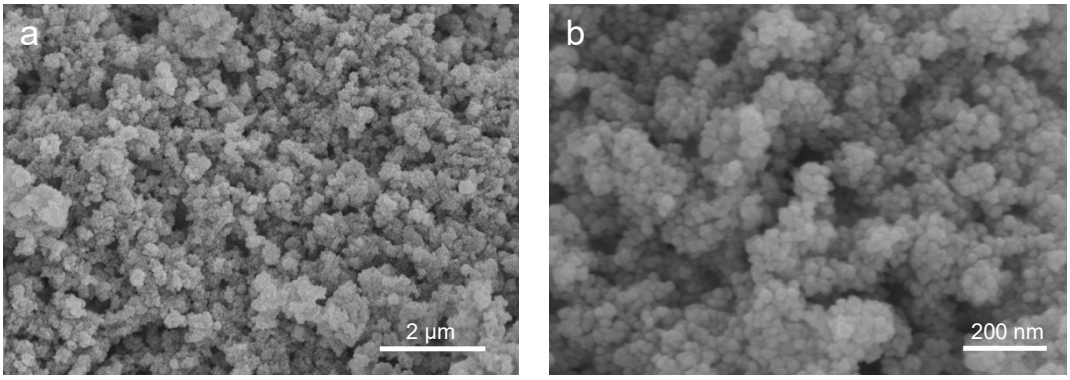

Fig. S2. (a) Low-magnified and (b) high-magnified SEM images of Ir_{SA}-Co_3O_4, respectively.

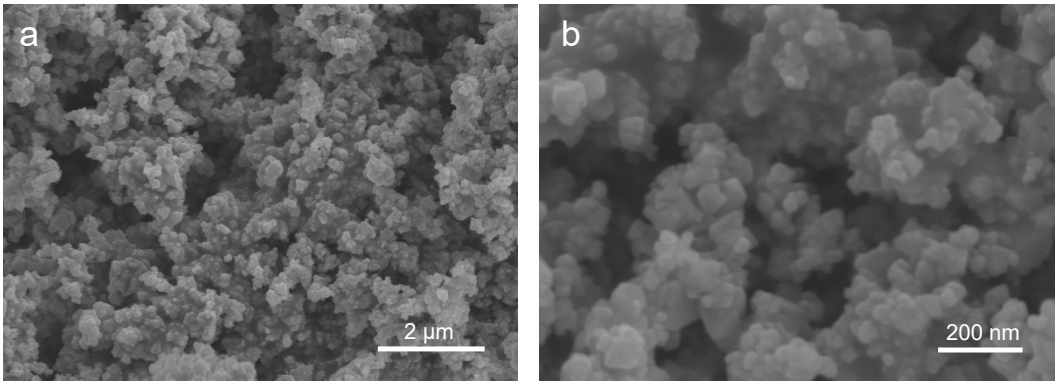

Fig. S3. (a) Low-magnified and (b) high-magnified SEM images of Ir_{ACSA}-Co_3O_4, respectively.

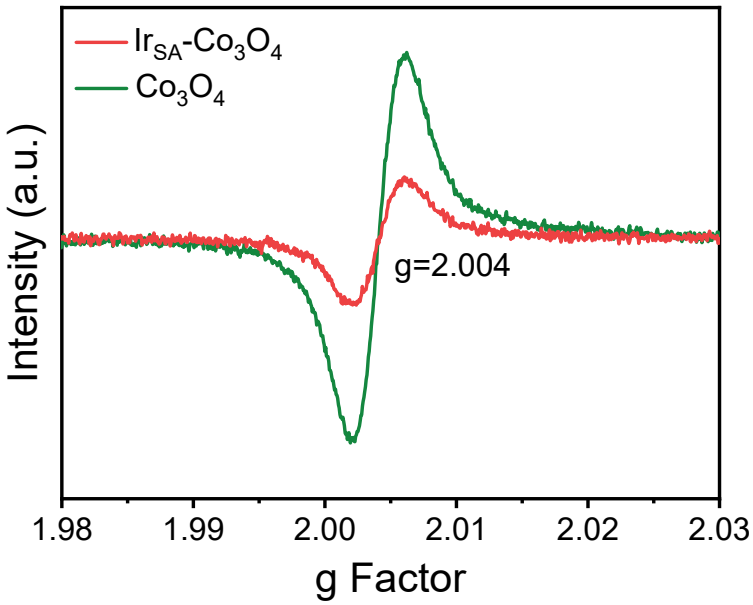

Fig. S4. EPR spectra of Ir_{SA}-Co_3O_4 and Co_3O_4.

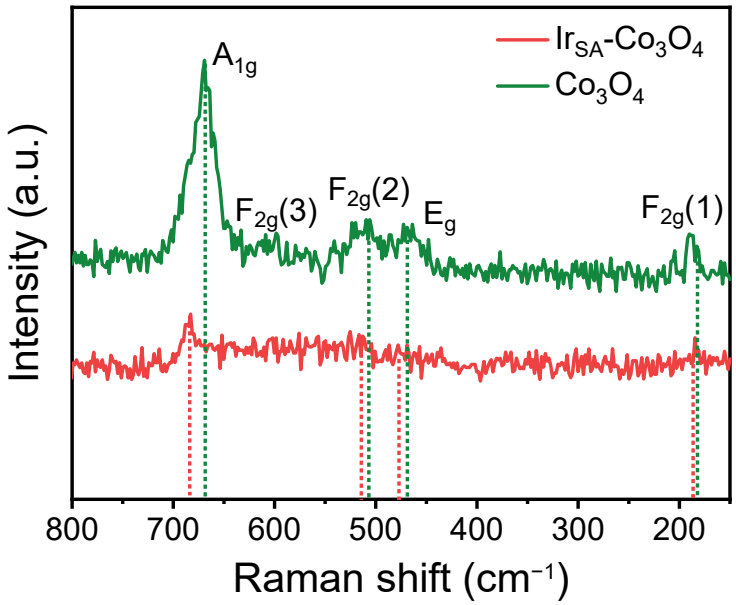

Fig. S5. Raman spectra of Ir_{SA}-Co_3O_4 and Co_3O_4.

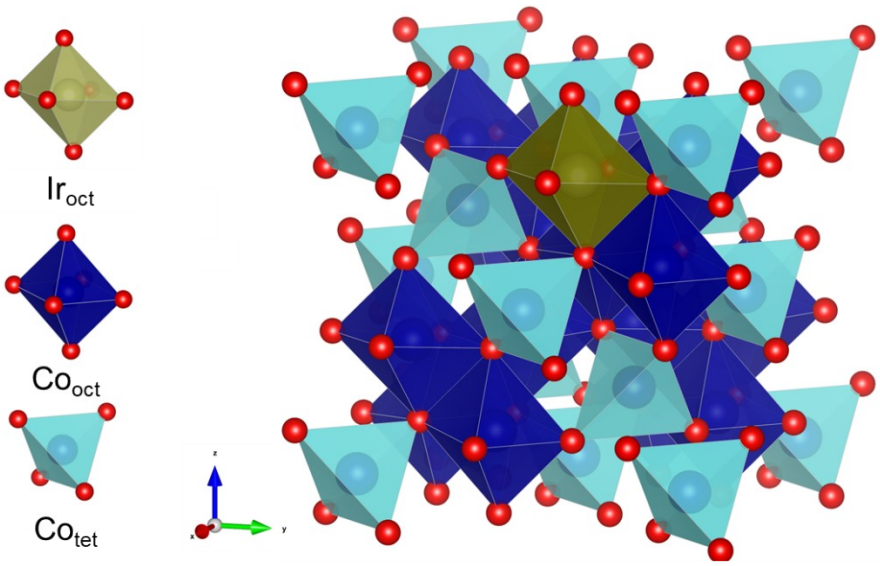

Fig. S6. Three-dimensional visualization of the topology illustration of Ir_{SA}-Co_3O_4.

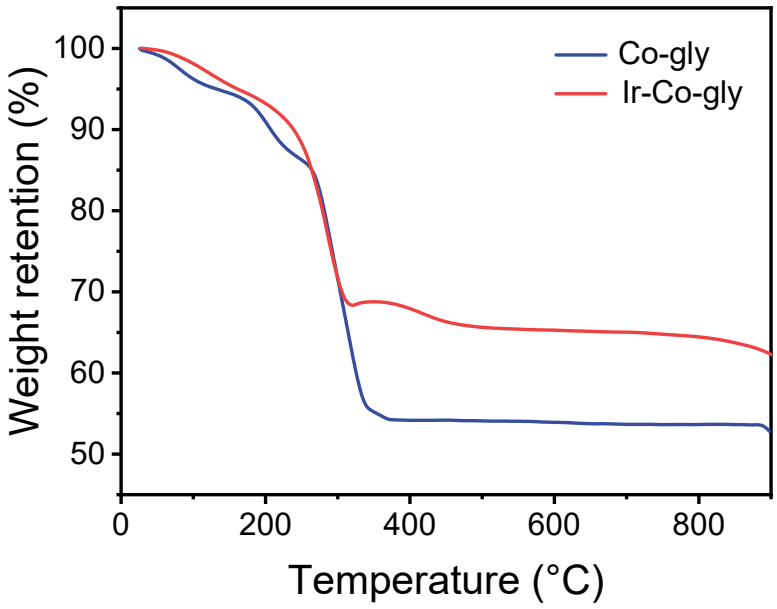

Fig. S7. TG curves of Co-gly and Ir-Co-gly precursors.

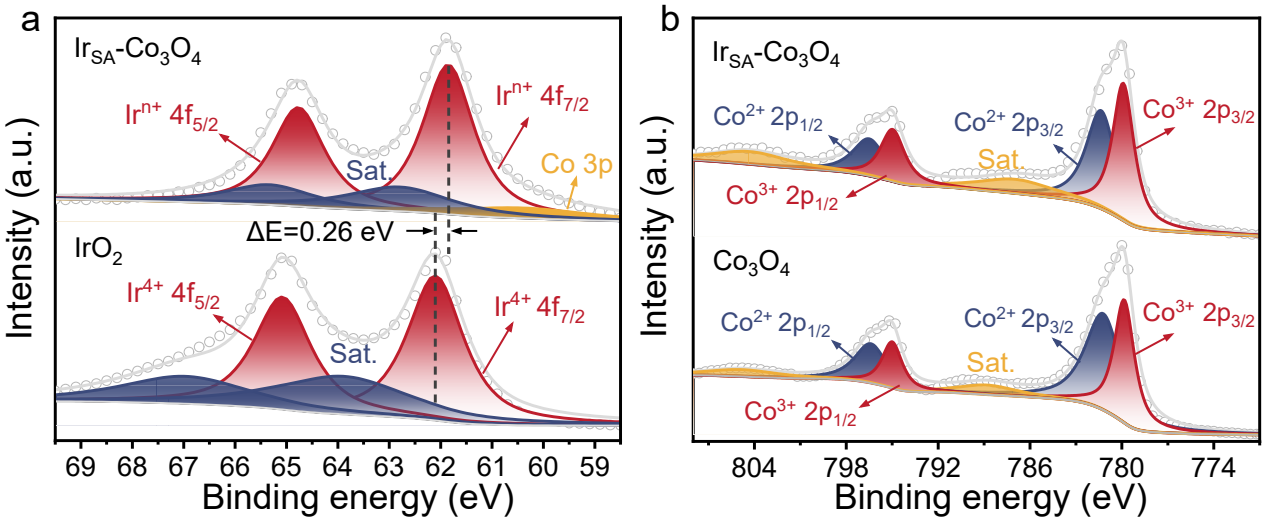

Fig. S8. (a) Ir 4f and (b) Co 2p XPS spectra of Ir_{SA}-Co_3O_4 and Co_3O_4.

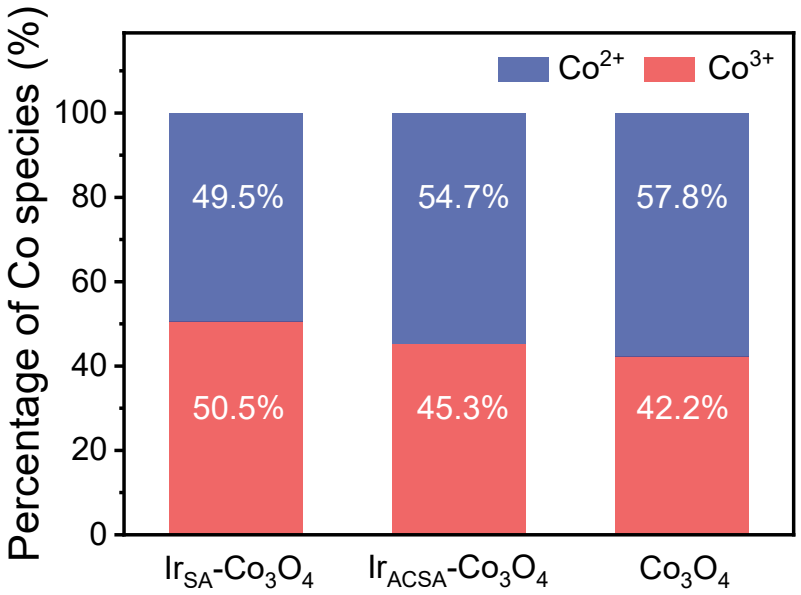

Fig. S9. Relative proportions of Co^{2+} and Co^{3+} in Ir_{SA}-Co_3O_4, Ir_{ACSA}-Co_3O_4, and Co_3O_4 obtained from XPS analysis.

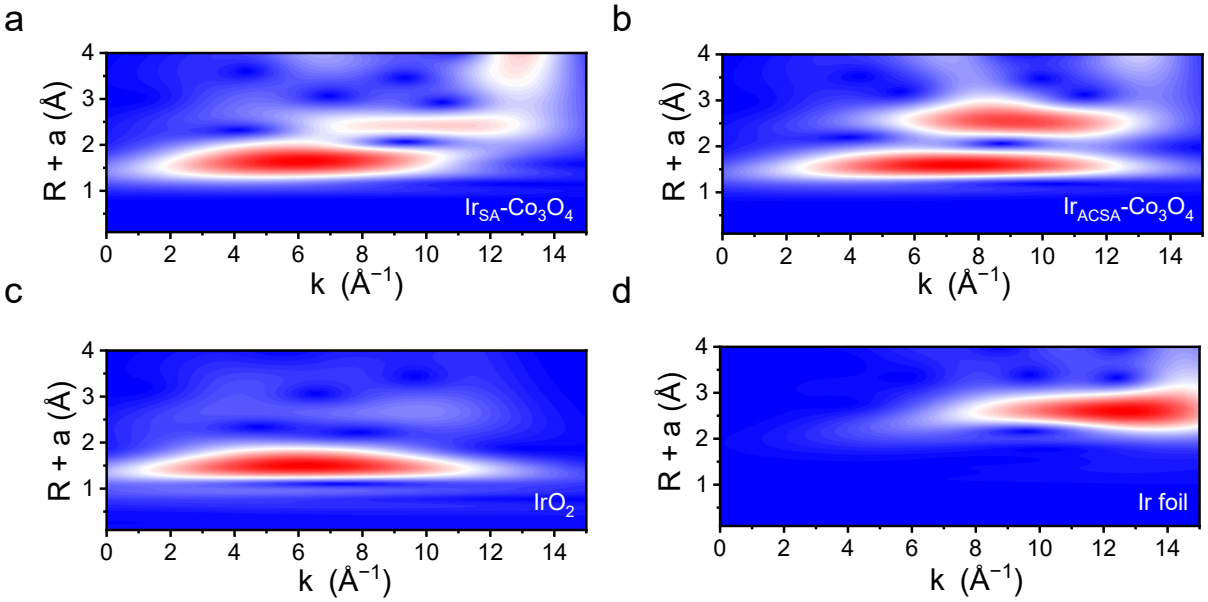

Fig. S10. (a-d) The corresponding Wavelet transform (WT) EXAFS of Ir_{SA}-Co_3O_4, Ir_{ACSA}-Co_3O_4, IrO_2, and Ir foil.

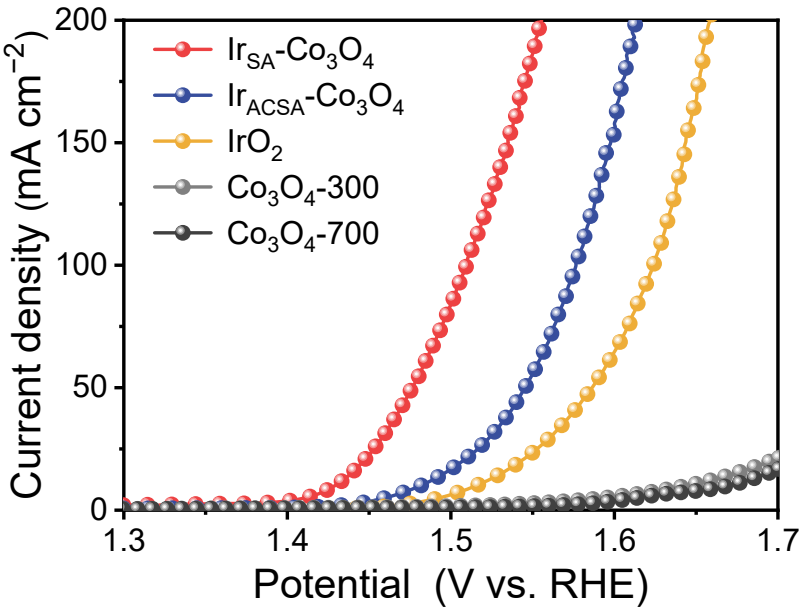

Fig. S11. LSV polarization curves of Ir_{SA}-Co_3O_4, Ir_{ACSA}-Co_3O_4, IrO_2, Co_3O_4-300, and Co_3O_4-700.

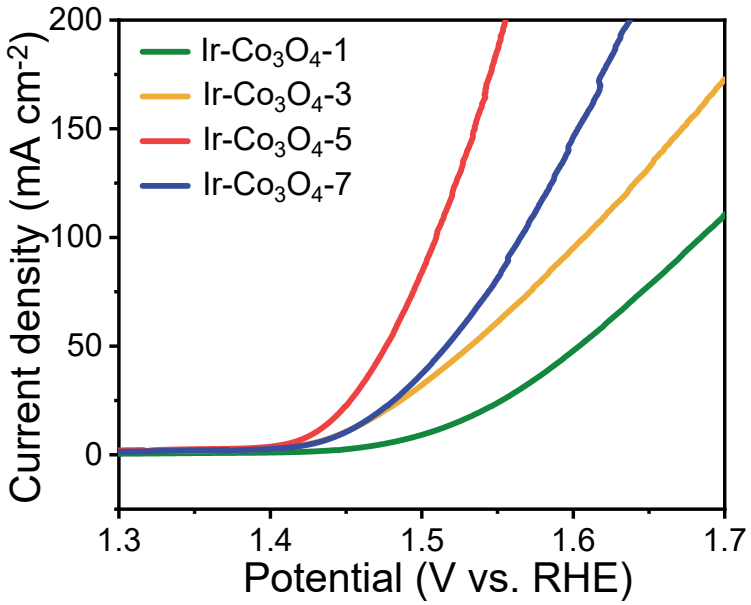

Fig. S12. LSV polarization curves of Ir-Co_3O_4-1, Ir-Co_3O_4-3, Ir-Co_3O_4-5, Ir-Co_3O_4-7.

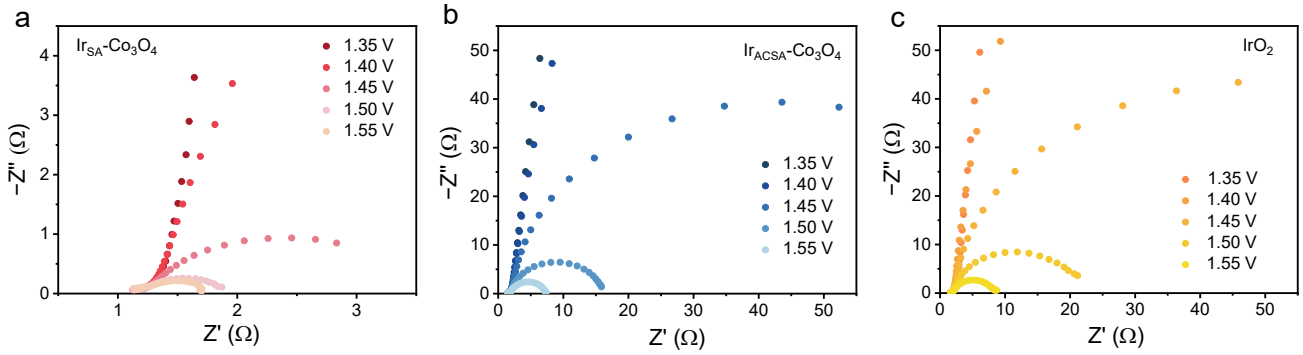

Fig. S13. (a-c) The corresponding Nyquist plots of Ir_{SA}-Co_3O_4, Ir_{ACSA}-Co_3O_4, and IrO_2 at different applied potentials.

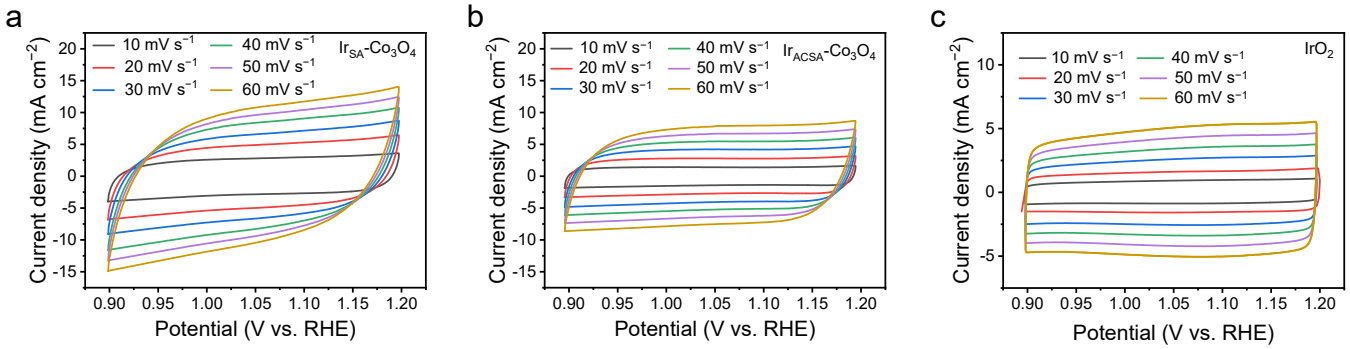

Fig. S14. Cyclic voltammograms of (a) Ir_{SA}-Co_3O_4, (b) Ir_{ACSA}-Co_3O_4, and (c) IrO_2 recorded at different scan rates (10, 20, 30, 40, 50, and 60 mV s^{-1}) within a potential window of 0.9−1.2 V vs RHE.

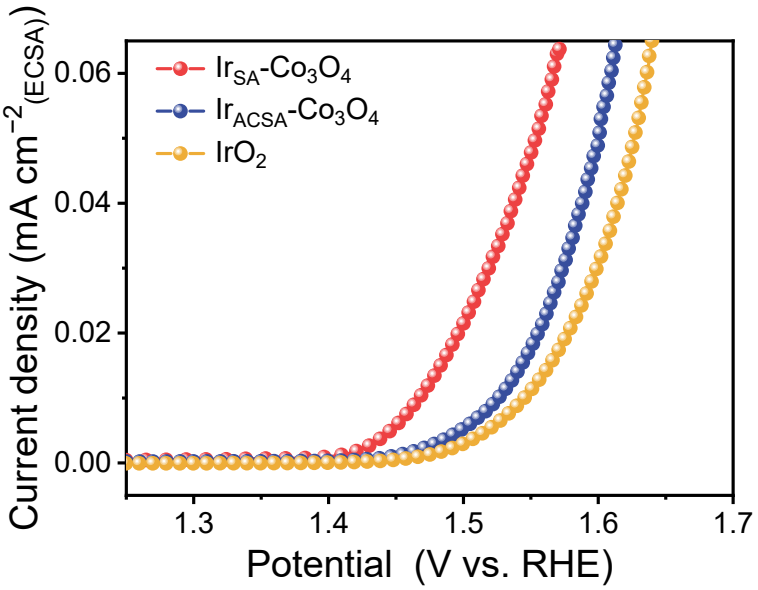

Fig. S15. ECSA-normalized OER polarization curves of Ir_{SA}-Co_3O_4, Ir_{ACSA}-Co_3O_4, and IrO_2.

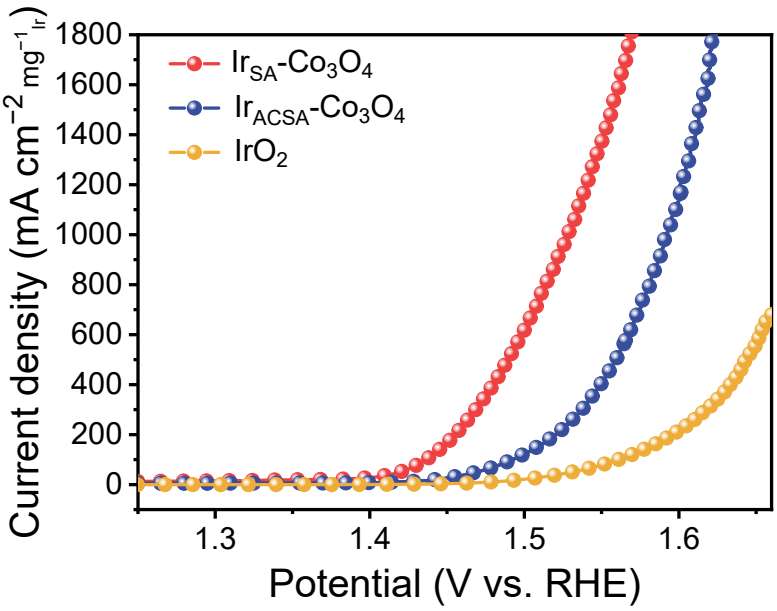

Fig. S16. Ir mass-normalized OER polarization curves of Ir_{SA}-Co_3O_4, Ir_{ACSA}-Co_3O_4, and IrO_2.

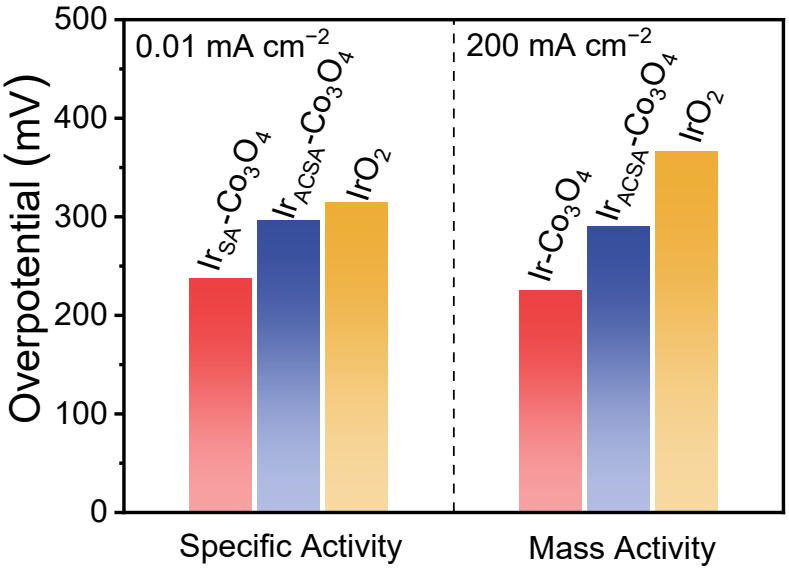

Fig. S17. Overpotential statistics at 0.01 mA cm^{-2} (left panel, specific activity) and 200 mA cm^{-2} (right panel, mass activity) for Ir_{SA}-Co_3O_4, Ir_{ACSA}-Co_3O_4, and IrO_2.

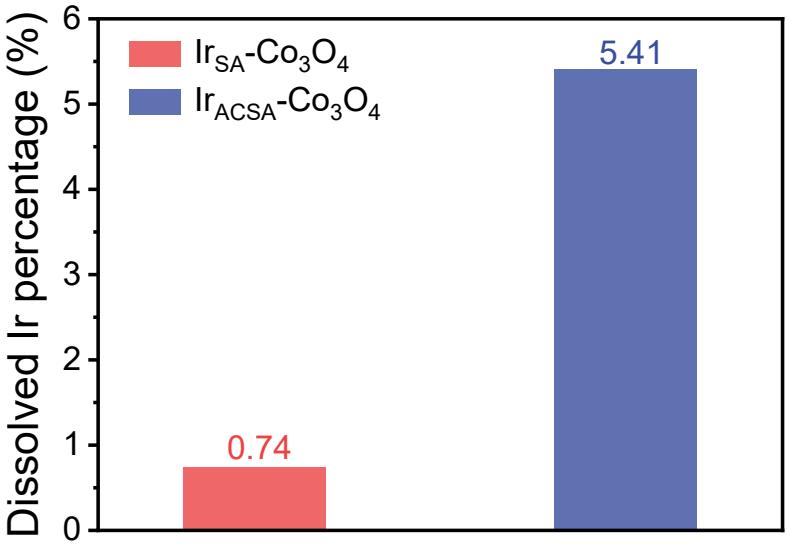

Fig. S18. Comparison of Ir dissolution percentages for Ir_{SA}-Co_3O_4 and Ir_{ACSA}-Co_3O_4 after stability test.

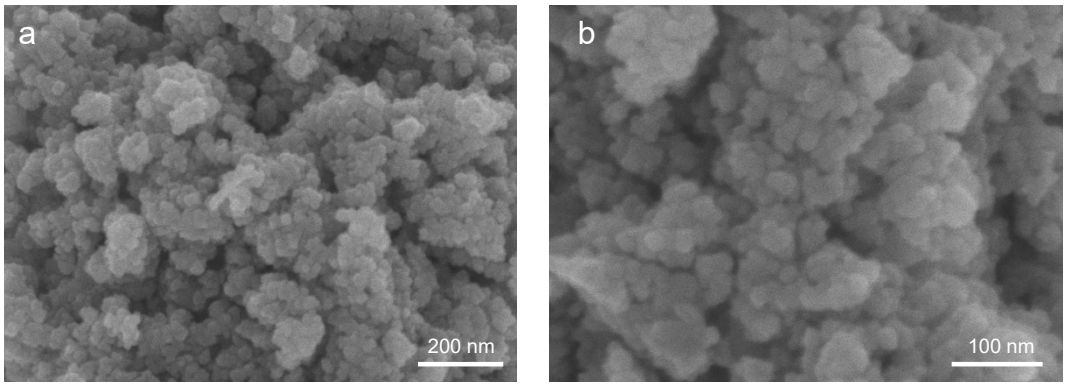

Fig. S19. (a) Low-magnified and (b) high-magnified SEM image of Ir_{SA}-Co_3O_4 after the stability test, respectively.

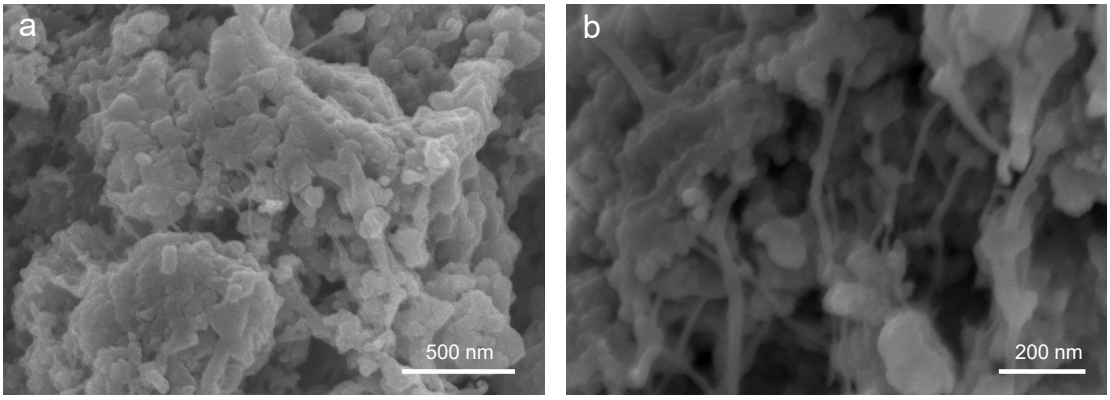

Fig. S20. (a) Low-magnified and (b) high-magnified SEM image of Ir_{ACSA}-Co_3O_4 after the stability test, respectively.

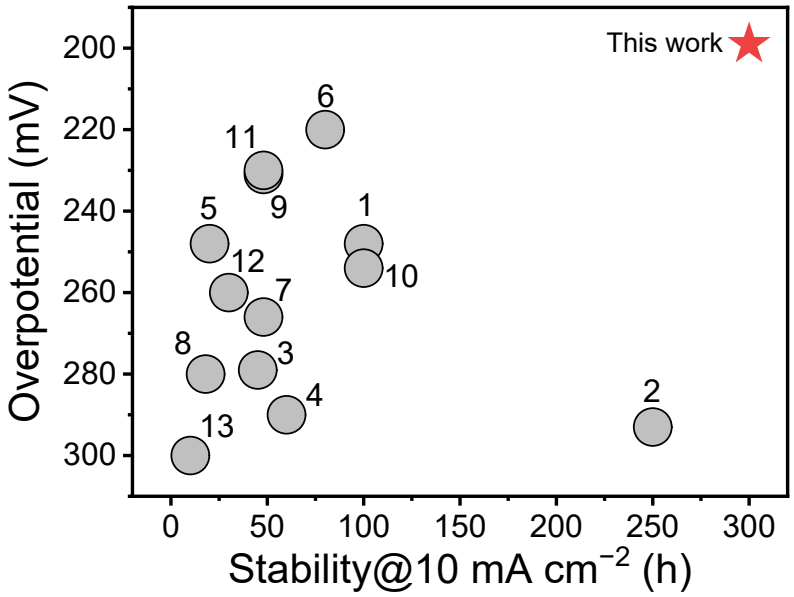

Fig. S21. Comparison of OER overpotentials and long-term durability with reported Ir-based catalysts.

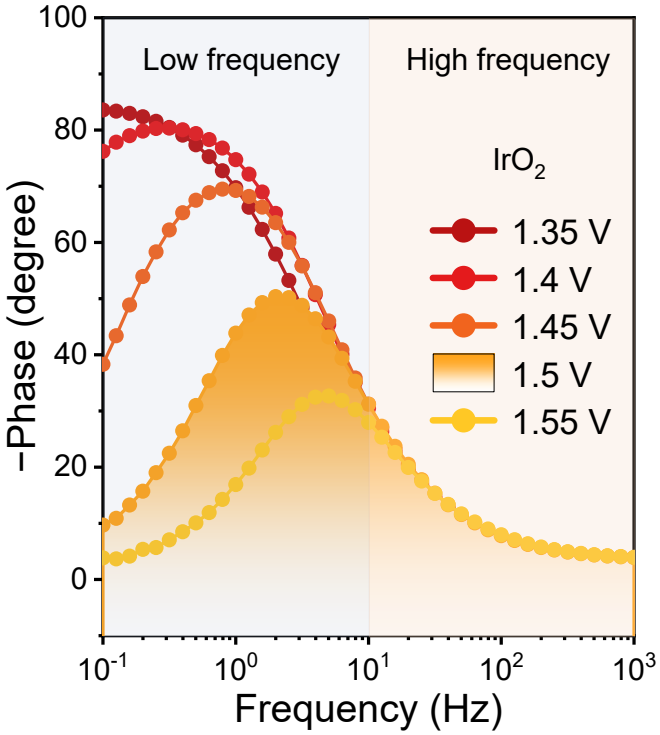

Fig. S22. Bode plots of IrO_2 at different applied potentials.

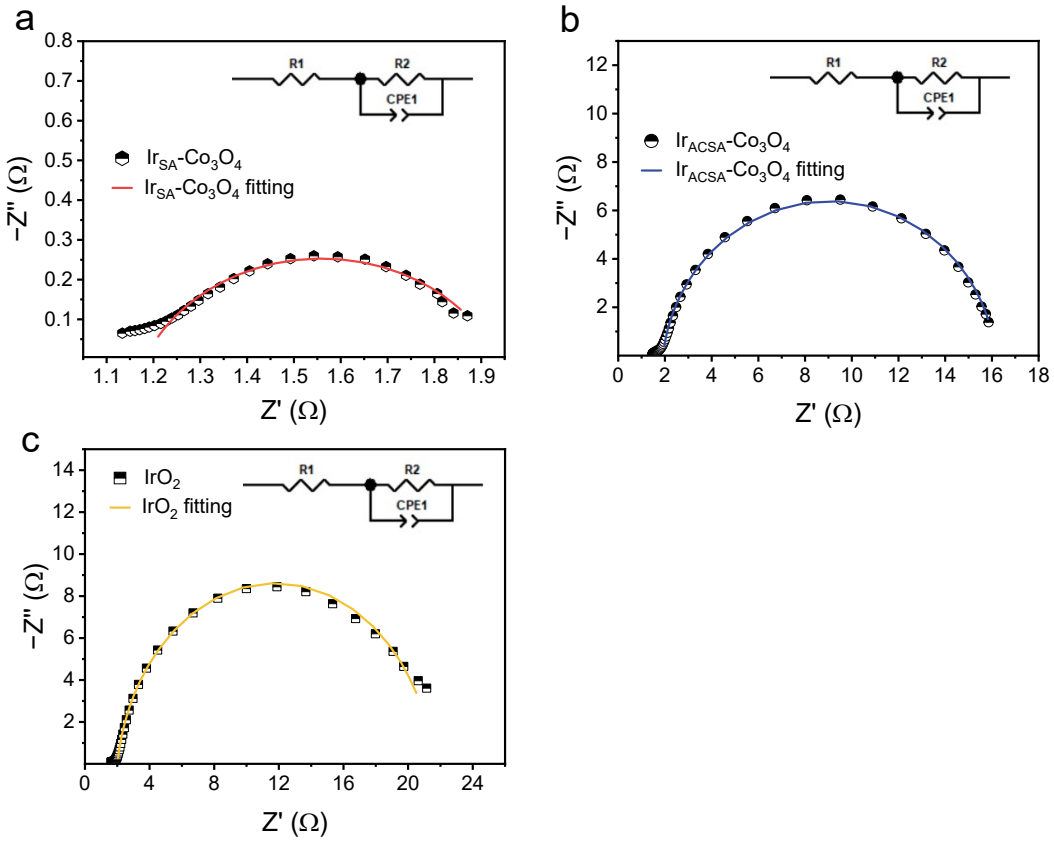

Fig. S23. (a-c) The corresponding Nyquist plots of Ir_{SA}-Co_3O_4, Ir_{ACSA}-Co_3O_4, and IrO_2 for OER. The inset shows equivalent circuit models for OER.

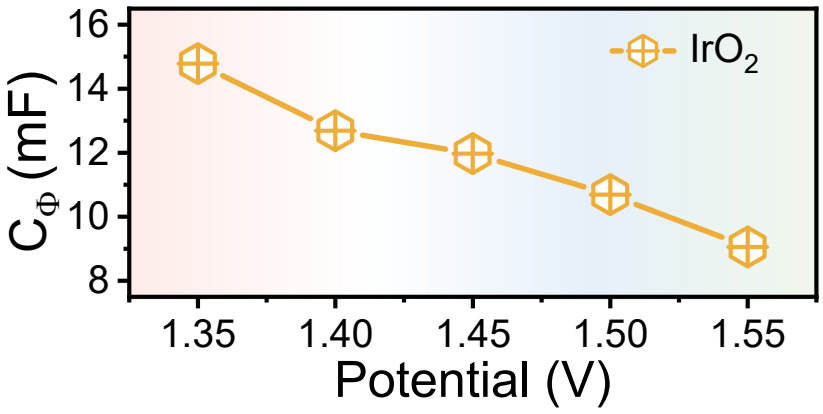

Fig. S24. Interfacial capacitance values of IrO_2 plotted against applied potentials.

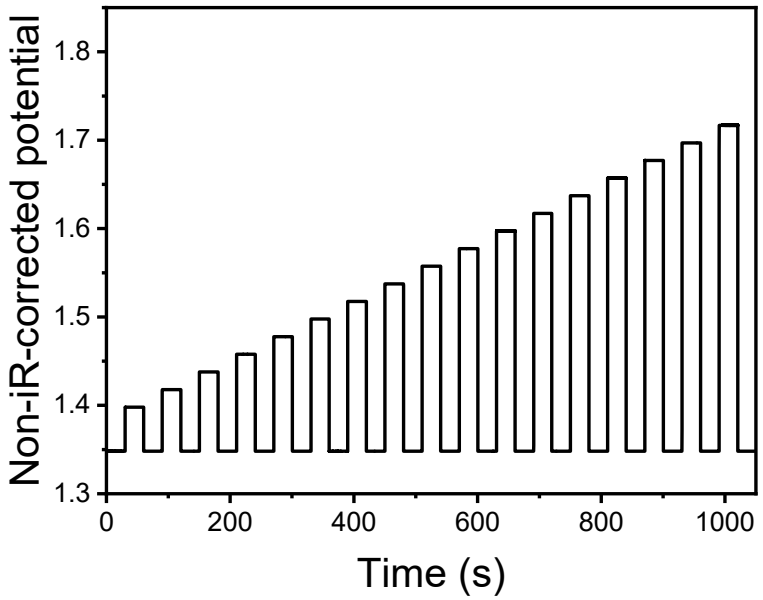

Fig. S25. Potential-time profile of pulse voltammetry measurements, with cathodic pulses at 1.35 V vs Ag/AgCl and anodic pulses ranging from 1.42 to 1.80 V vs Ag/AgCl.

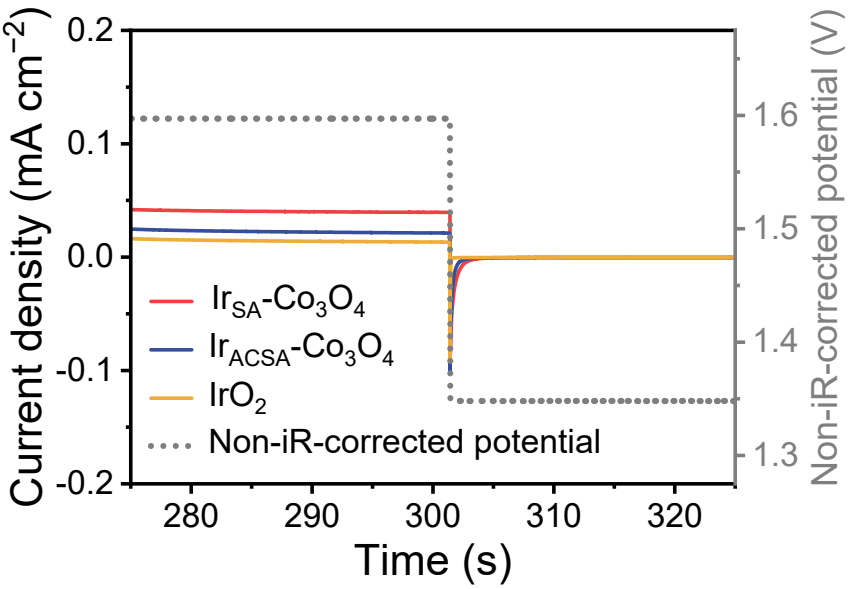

Fig. S26. Representative pulse voltammetry showing transitions from oxidation potential to open-circuit potential (OCP) and the corresponding pulse current response.

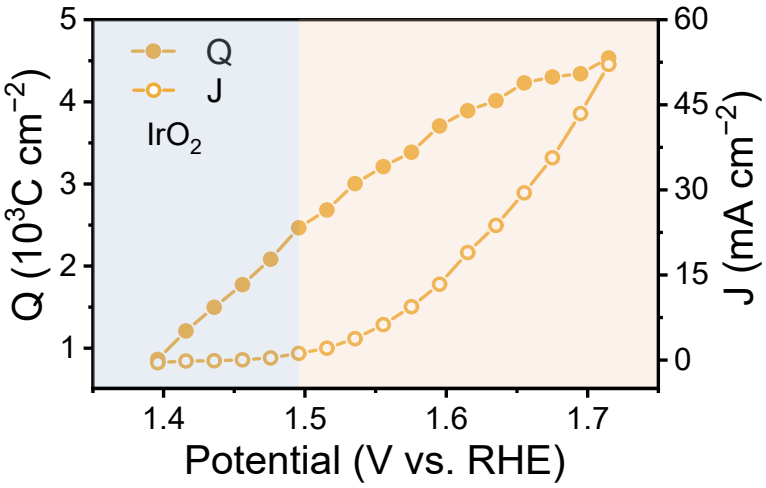

Fig. S27. Pulse voltammetry measurements of IrO_2.

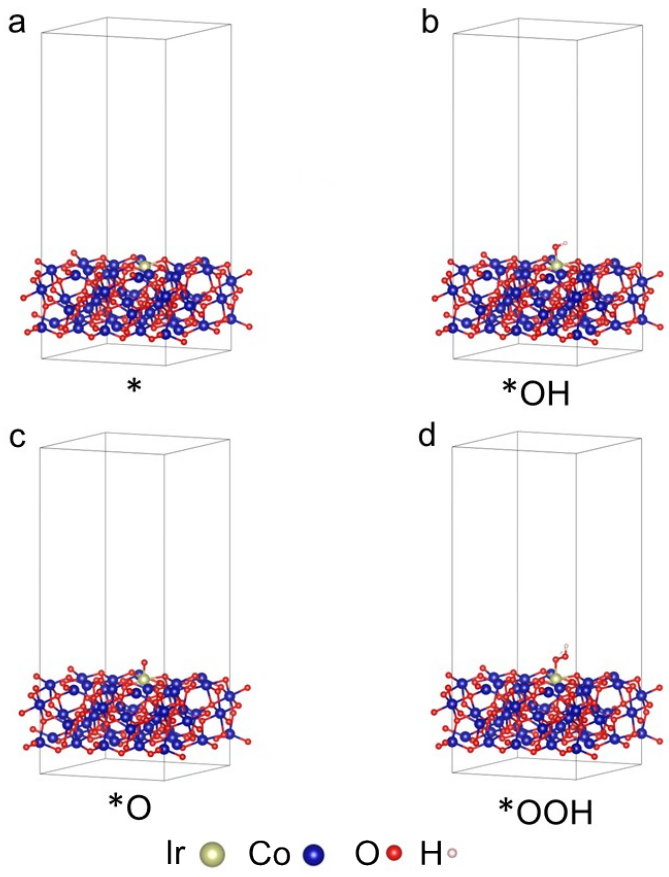

Fig. S28. Structures of (a) pure surface, (b) *OH, (c) *O, (d) *OOH intermediates adsorbed on Ir_{SA}-Co_3O_4.

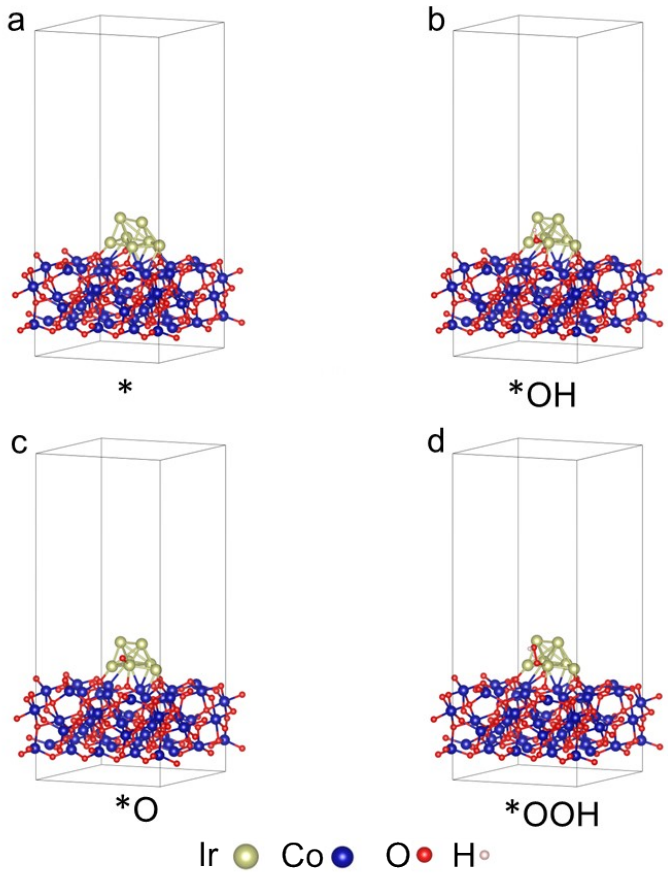

Fig. S29. Structures of (a) pure surface, (b) *OH, (c) *O, (d) *OOH intermediates adsorbed on Ir_{AC}-Co_3O_4.

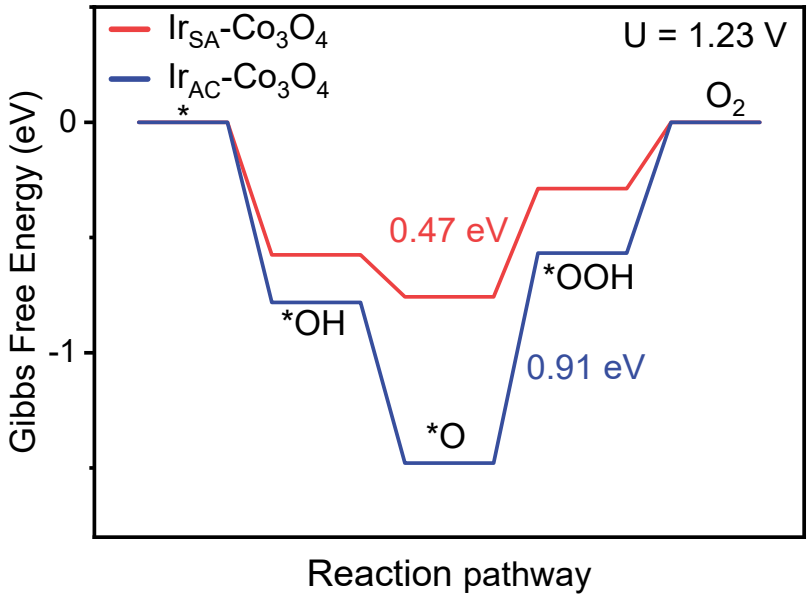

Fig. S30. The hypothetical AEM pathways of four-electron-based acidic OER at U = 1.23 V.

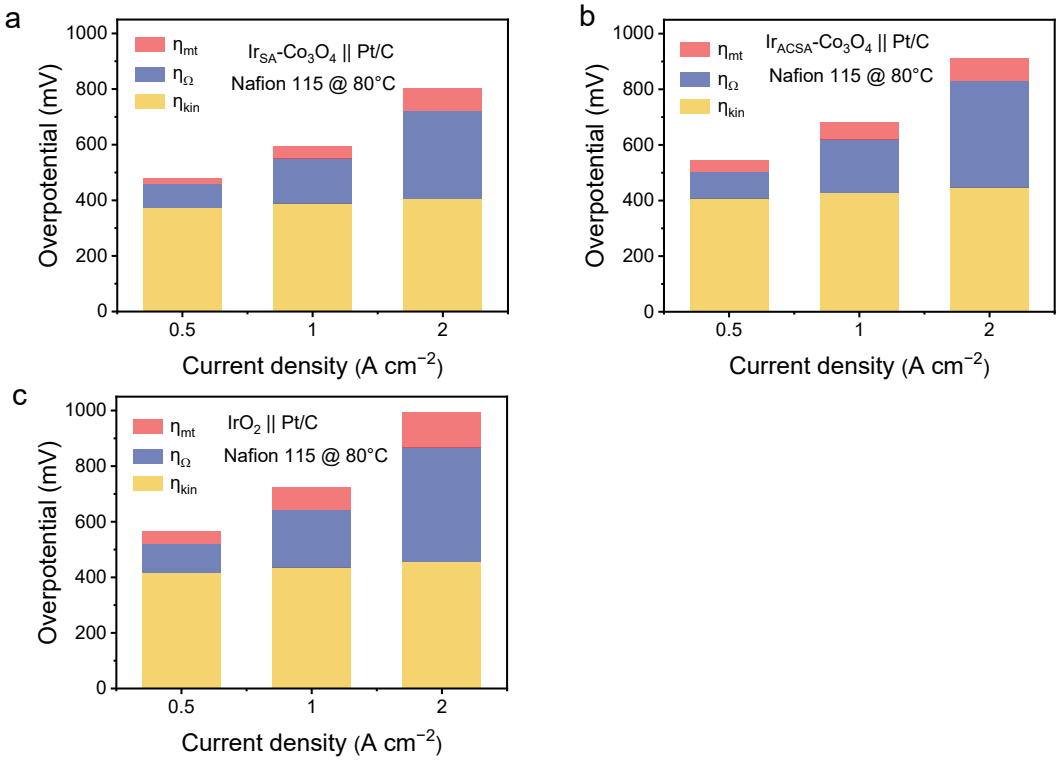

Fig. S31. Overpotential analysis of PEMWE cells with (a) Ir_{SA}-Co_3O_4‖Pt/C, (b) Ir_{ACSA}-Co_3O_4‖Pt/C, and (c) IrO_2‖Pt/C at different current densities, showing the statistical contributions from kinetic, ohmic, and mass transport losses.

Table S1 Molar ratios of Ir and Co in the catalysts determined by ICP analysis

Catalyst	Ir mass fraction (%)	Atomic ratio (Ir/Co)
Ir_{SA}-Co_3O_4	7.72	18:1
Ir_{ACSA}-Co_3O_4	7.80	18:1
IrO_2	85.70	/

Table S2 Comparison of OER overpotentials and long-term durability with reported Ir-based catalysts. (j = 10 mA cm^{-2}).

Catalyst	Electrolyte	Overpotential (mV)	Stability (h)	Reference
Ir_{SA}-Co_3O_4	0.5 M H_2SO_4	199	300	This work
H-Ir@Co_3O_4	0.5 M H_2SO_4	248	100	J. Am. Chem. Soc., 2025, 147, 16, 13345–13355
IrO_x/TiN	0.1 M $HClO_4$	293	250	J. Am. Chem. Soc., 2024, 146, 16499–16510.
O-IrVMn/IrO_x	0.1 M $HClO_4$	279	45	J. Am. Chem. Soc., 2024, 146, 19327−19336
Ir/$Cu_{0.3}Co_{2.7}O_4$	0.1 M $HClO_4$	290	60	Nat. Commun., 2024, 15, 1767
$IrB_{1.1}$	0.5 M H_2SO_4	248	20	Angew. Chem. Int. Ed., 2024, 63, e202407577
Cu_2IrO_x-AE	0.5 M H_2SO_4	220	80	Adv. Mater., 2024, 36, 2312140.
KIr_4O_8	0.5 M H_2SO_4	266	48	Adv. Mater., 2024, 36, 2402643
Ir/D-ATO	0.05 M H_2SO_4	280	18	Nat. Commun., 2023, 14,5402
IrO_x	0.5 M H_2SO_4	231	48	Angew. Chem. Int. Ed., 2023, e202313954.
Ti-IrOx/Ir	0.5 M H_2SO_4	254	100	Chem., 2023, 9, 2931–2942.
IrO_x/9R-$BaIrO_3$	0.5 M H_2SO_4	230	48	J. Am. Chem. Soc., 2021, 143, 18001–18009
IrO_x/GDY	0.5 M H_2SO_4	260	30	Adv. Energy Mater., 2021, 2101138
Li-IrO_x	0.5 M H_2SO_4	300	10	J. Am. Chem. Soc., 2019, 141, 3014−3023

References

[1] G. Kresse, and J. Furthmüller, Efficient iterative schemes for ab initio total-energy calculations using a plane-wave basis set, Physical Review B, 1996, **54**, 11169-11186.

[2] P. E. Blöchl, Projector augmented-wave method, Physical Review B, 1994, **50**, 17953-17979.

[3] J. P. Perdew, K. Burke, and M. Ernzerhof, Generalized Gradient Approximation Made Simple, Physical Review Letters, 1996, **77**, 3865-3868.